Localization of CuO, NiO, and Co_3O_4 sintering additives in dense proton-conducting perovskite ceramics based on $BaSnO_3$

George N. Starostin[1,2], Mariam T. Akopian[1,2], Gennady K. Vdovin[1], Inna A. Starostina[1,2*], Dmitry A. Medvedev[1,2*]

[1] Laboratory of Electrochemical Devices Based on Solid Oxide Proton Electrolytes, Institute of High-Temperature Electrochemistry, 620137 Yekaterinburg, Russia
[2] Hydrogen Energy Laboratory, Ural Federal University, 620002 Yekaterinburg, Russia
* Corresponding authors: Dmitry Medvedev, email: dmitrymedv@mail.ru, ORCID: 0000-0003-1660-6712; Inna Starostina, email: fair696@yandex.ru, ORCID: 0000-0002-9793-1375.

Abstract

Sintering additives have been widely employed to achieve good sinterability of barium-based proton-conducting perovskites (based on $BaZrO_3$, $BaCeO_3$, $BaTiO_3$, $BaHfO_3$, $BaThO_3$, and $BaSnO_3$). This is of particular importance for the fabrication of multilayered ceramic cells, in which the thin-film electrolyte layer can be primarily densified at relatively low sintering temperatures (1350–1500 °C). The introduction of sintering additives facilitates the fabrication of gas-tight ceramics; however, the precise nature of their localization and their effects on the functional properties remain uncertain and even questionable. In this study, we present a comprehensive characterization of ceramic materials based on Y-doped $BaSnO_3$ prepared with the addition of three sintering additives (copper, cobalt, and nickel oxides) at 1 wt%. Although these introduced oxides belong to a group of compounds with similar physicochemical properties, each additive exerts a distinct influence on the microstructural and electrochemical properties of the ceramics owing to their own chemical localization features. These features are discussed in detail in the present work, providing useful information in the field of using sintering additives for the preparation of oxide ceramics for high-temperature applications.

Keywords: $BaSnO_3$; perovskite; protonic transport; sintering additive; PCFCs; SOFCs; conductivity

Graphical abstract

1. Introduction

The increasing global demand for energy and the need to reduce reliance on fossil fuels have emerged as significant concerns in recent years. As an alternative approach, the development of renewable technologies for electricity generation, including the utilization of so-called "green" hydrogen, is being actively promoted [1–3]. Among these technologies, solid oxide fuel cells (SOFCs) exhibit one of the highest potentials for direct chemical energy conversion, using a variety of hydrogen-based fuels to generate electrical power with high efficiency [4–7]. Although SOFCs based on traditional oxygen-ion YSZ electrolytes have been successfully tested over a long-term period and commercially exploited in both portable and stationary applications, several limitations exist in the further development of such devices. These include challenges related to the selection of compatible functional materials, long-term degradation, and high production costs [8–10]. These issues can be overcome by reducing the SOFC operating temperature by replacing the oxygen-ion electrolytes with proton-conducting electrolytes [11–13].

Among protonic conductors, barium-containing perovskites are considered the most promising state-of-the-art materials, i.e., acceptor-doped $BaCeO_3$, $BaZrO_3$, their solid solutions, $BaHfO_3$, $BaThO_3$, and $BaSnO_3$ [14–18]. For their use as SOFC electrolytes, gas-tight thin-film ceramic membranes need to be formed to prevent non-electrochemical mixing of both anode and cathode gases. However, the fabrication of dense barium-based electrolyte ceramics is technologically challenging due to the refractory nature of these materials. One way could be the synthesis of nanopowders followed by sintering them into ceramics at high temperatures (~1700 °C). Although this approach is suitable for the preparation of individual (bulk) ceramic samples, much lower sintering temperatures are required to avoid electrode densification, barium evaporation, and the formation of low-conductivity phases at the electrolyte–electrode interface when multilayer structures are being fabricated [19,20]. Another economically feasible and simple approach utilizes a low concentration of sintering additives [21,22]. The introduction of these materials can reduce the sintering temperature by 100–400 °C to fabricate dense ceramics. The high density of the

ceramic samples at lower sintering temperatures is associated with the appearance of low-melting phases that promote diffusion processes in a ‘solid–liquid’ system.

Despite the positive effect of sintering additives on ceramic sinterability, they can negatively contribute to the electrical conductivity at the same time. In particular, the well-studied NiO sintering additive can interact with the electrolyte material to form a low-conductivity BaY_2NiO_5 phase [23–27]. This impurity contaminates the grain boundaries of an electrolyte, reducing its electrical conductivity. Kim et al. [27], using monitoring electrical conductivity relaxation, reported that the proton conductivity decreases with increasing NiO concentration. The observed effects are related to the degradation of hydration kinetics and defect-chemical parameters. The latter include a reduction in proton mobility, an increase in hole conductivity and a narrowing of the electrolytic domain for the Ni-containing electrolytes. Cobalt, copper, and zinc oxides are also effective sintering additives for the densification of Ba-containing proton conductors [28]. The few published studies on such additives mainly report a comparative analysis of the transport properties of ceramics produced with different concentrations of sintering additives. The localization of sintering additives in the ceramic microstructure has been poorly investigated, although these findings could be useful in mitigating the negative effects of additives.

In the present work, the impact of sintering additives on the microstructure and transport properties of Ba-containing proton-conducting ceramics was thoroughly studied using barium stannate as a model material. For this purpose, dense $BaSn_{0.8}Y_{0.2}O_{3-\delta}$ samples were prepared using 1 wt% CuO, NiO, and Co_3O_4 sintering additives. The actual concentration of the introduced impurities was determined via a combination of energy dispersive analysis and mass spectrometry techniques. Furthermore, we attempted to determine the localization of sintering additives. For this purpose, the elemental composition of polished freshly prepared samples was identified, the samples were subsequently reduced in a hydrogen atmosphere, and the mechanism of impurity extraction was investigated.

2. Experimental

The $BaSn_{0.8}Y_{0.2}O_{3-\delta}$ (BSY) powder was prepared via the conventional solid-state synthesis route using $BaCO_3$ (99.98% Sigma–Aldrich, USA), SnO_2 (99.9% Sigma–Aldrich, USA), and Y_2O_3 (99.9% Sigma–Aldrich, USA) as starting reagents. Stoichiometric amounts of the dried precursors were ground and mixed in acetone medium for 2 h via YSZ milling balls via a planetary ball mill (Pulverizette 7 premium line, FRITSCH, Germany). The mixture was sieved, dried, and calcined at 1200 °C for 5 h. The obtained powder was then thoroughly mixed with 1 wt.% CuO (99.99% Sigma–Aldrich, USA), NiO (99% Alfa Aesar, USA) or Co_3O_4 (99.7% Alfa Aesar, USA), uniaxially cold-pressed at 140 MPa into cylindrical samples denoted BSY-Cu, BSY-Ni, and BSY-Co, respectively. Finally, the pressed samples were sintered at 1500 °C for 5 h in ambient air. The pristine $BaSn_{0.8}Y_{0.2}O_{3-\delta}$ pellets were also sintered at 1350, 1400 or 1500 °C. One of the pristine samples was covered with a sacrificial powder of the same composition to prevent BaO evaporation and then calcined at 1600 °C for 5 h.

X-ray diffraction (XRD, Rigaku Co. Ltd., Japan) with Cu Kα radiation (λ = 1.54056 Å) was utilized for phase analysis. The data were collected over a 2θ range of 10°–90° with a scanning step of 0.01° and a scanning rate of 0.3° min−1. The phase composition was determined through the ICDD PDF-2 database, while structural parameters were calculated via Rietveld refinement analysis via FullProf software.

The surface morphology was examined via a scanning electron microscope (TESCAN MIRA III, TESCAN s.r.o., Czech Republic) equipped with a Schottky cathode with an accelerating voltage of 15 keV at a current of 300 pA. The grain size parameters of the ceramic samples were measured by processing the obtained micrographs with GrainD software [29]. Energy dispersive X-ray (EDX) spectroscopy analysis was performed with an instrument from Oxford Instruments. Elemental mapping images were obtained via Aztec software.

The weight fraction of the sintering aid was determined via inductively coupled plasma–mass spectrometry (ICP-MS) on a NexIon 2000 instrument (Perkin Elmer, USA). The ceramic powder was dissolved in diluted hydrochloric acid (20 wt.%) at

100 °C. The resulting solution was also diluted with deionized water to achieve a concentration of 10–100 μg dm^{-3} for the determination of elements in the solution and then analysed. The spectrometer was calibrated with Ni, Co, and Cu single-element samples (PerkinElmer Pure Grade Aqueous Standards, USA). The arithmetic average of three parallel measurements was taken as the analysis result.

The electrical transport properties of the obtained ceramic samples were investigated via electrochemical impedance spectroscopy (EIS). The polished ceramic samples were coated on both sides with Ag paste and then heat-treated at 800 °C for 1 h to form symmetrical electrodes. The impedance spectra were recorded in a frequency range from 0.1 Hz to 1 MHz in a wet air atmosphere (pH_2O = 0.03 atm) via an Amel 2550 potentiostat/galvanostat (Italy) connected to a Materials M520 frequency response analyser (Italy) for every 50 °C while cooling from 600 to 250 °C. The obtained data were analysed via a Voight-type equivalent circuit via ZView software (Scribner Associates, Inc.).

SEM was also employed to investigate the exsolution behavior of the sintering additive particles after reduction tests. First, the polished samples were placed in a tube furnace and heated in an ambient air atmosphere to 700 °C. Next, the feeding gas was replaced with humid hydrogen when the samples were held at 700 °C for 10 h and then cooled at a rate of 5° min^{-1}. A hydrogen humidity of 3 vol.% was set by passing H_2 through a water bubbler thermostated at 25 °C.

3. Results and Discussion

3.1. Preparation of BSY dense ceramics

Barium stannate ($BaSnO_3$) and barium zirconate ($BaZrO_3$) materials are very similar in terms of their sinterability, as the preparation of the corresponding ceramics presents a significant challenge. For example, barium zirconate ceramics are usually formed in two steps: presynthesis and subsequent sintering at very high temperatures. Schober and Bohn [30] obtained Y-doped $BaZrO_3$ by annealing at 1250 °C for 10 h followed by sintering at 1715 °C for 30 h. Iguchi et al. [31] employed similar temperatures, but the exposure time dramatically increased to 40 h during synthesis

and 200 h during the sintering process. Duval et al. [32] used even higher temperatures (up to 1400 and 2200 °C) for the synthesis and sintering of zirconate ceramics.

According to the available literature, solid-state synthesis is the most common method for the preparation of doped $BaSnO_3$ ceramics [17]. Moreover, very high sintering temperatures (1500–1600 °C) have been employed to attain the desired degree of densification in stannate ceramics. Notably, the preparation of barium stannate-based materials via wet chemistry approaches is constrained by the high cost and complexity of producing tin-containing precursors. Moreover, the most readily available $SnCl_2$ precursor can introduce chlorine into the structure of the target oxides, which can impact their functional properties. Therefore, the solid-state synthesis route remains the most technologically straightforward and cost-effective.

The present study employed conventional solid-state synthesis to analyse the phase composition evolution of stannate materials. To achieve this goal, a $BaSn_{0.8}Y_{0.2}O_{3-\delta}$ powder was initially synthesized at 1200 °C and then sintered at different temperatures ranging from 1300 to 1600 °C. **Figure 1** shows the corresponding XRD patterns. The initial synthesis at 1200 °C resulted in incomplete formation of the target perovskite phase: the XRD pattern revealed a number of reflections related to the starting reagents, Y-enriched and Y-deficient barium stannate phases, and trace amounts of intermediate $Ba_3Y_4O_9$ and $Ba_3Sn_2O_7$ phases. The target phase, with a lattice parameter of 4.168±0.006 Å, formed during the second heat treatment starting at 1350 °C. Moreover, the concentration of undesirable phases decreases as the sintering temperature increases. The attainment of a single-phase state for $BaSn_{0.8}Y_{0.2}O_{3-\delta}$ was achieved at 1500 °C, showing that phase formation in stannates is quite complex in the case of the solid-state synthesis route. These findings are in accordance with the phase relationships observed in barium zirconate materials, as previously discussed.

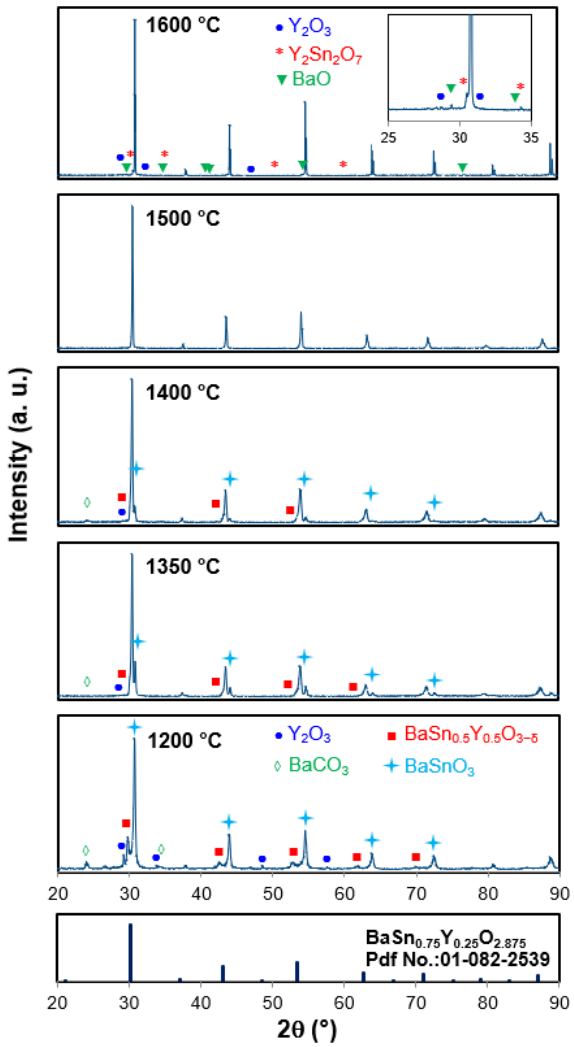

Figure 1. XRD patterns of the pristine $BaSn_{0.8}Y_{0.2}O_{3-\delta}$ pellets calcined at 1200–1600 °C in ambient air and the corresponding ICDD PDF-2 card for Y-doped $BaSnO_3$.

As evidenced by the microstructure studies, the $BaSn_{0.8}Y_{0.2}O_{3-\delta}$ sample sintered at 1500 °C displays a porous microstructure with regions of fine grain segregation, as shown in **Figure 2**. Given that the relative density attained was only 60% of the theoretical value, the sintering temperature was subsequently increased to 1600 °C (for 5 h) with the aim of obtaining a denser ceramic. However, this resulted in only a negligible increase in the material density (up to 65%), confirming that stannate materials are particularly susceptible to sintering difficulties. Furthermore, the target phase decomposed, accompanied by the formation of Y-deficient barium stannate and a number of impurities, when the ceramic was sintered at 1600 °C. This phenomenon may be associated with minor barium evaporation (despite the use of sacrificial powder), as well as the possible exsolution of Y_2O_3 from the perovskite structure, which may interact with tin to form a $Y_2Sn_2O_7$ pyrochlore phase. A recent study

revealed the presence of similar pyrochlore phases ($Ln_2Sn_2O_7$) at elevated dopant concentrations [33], indicating that these phases may exhibit greater thermodynamic stability than the perovskite phase does, particularly in the context of Ba deficiency.

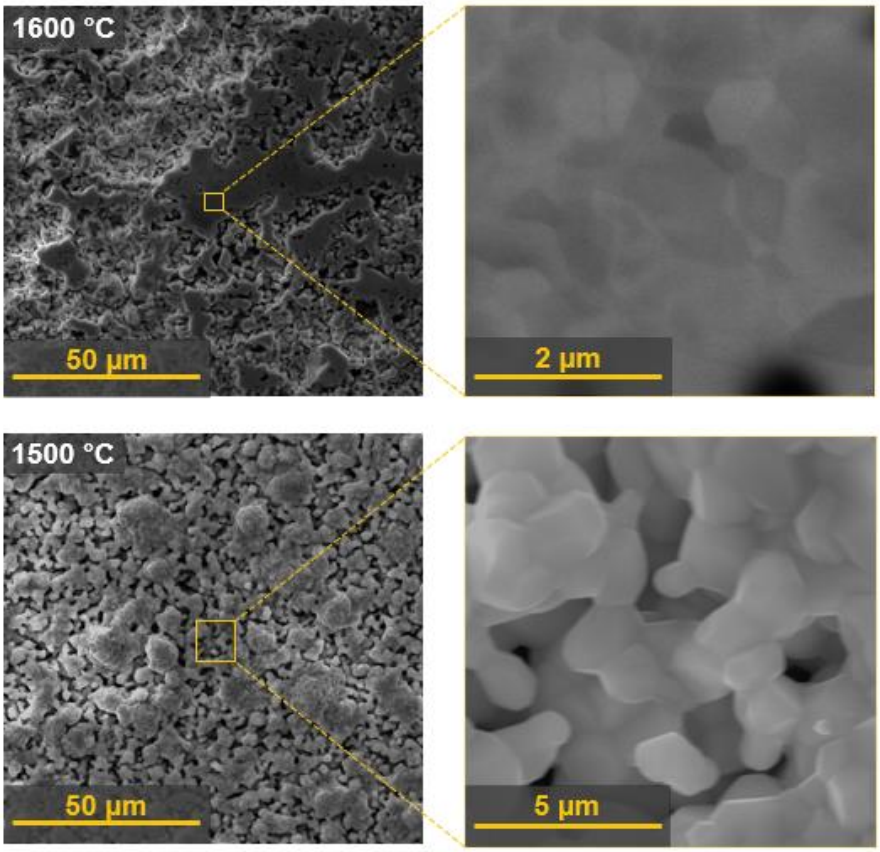

Figure 2. SEM image of pristine $BaSn_{0.8}Y_{0.2}O_{3-\delta}$ ceramic samples calcined at 1500 and 1600 °C for 5 h in ambient air.

According to the provided analysis, the fabrication of dense and gas-tight $BaSnO_3$-based ceramics at rational sintering temperatures is a challenging process when the solid-state synthesis method is employed. One of potential solutions to this issue is the addition of sintering additives at very small concentrations. To ascertain which of these additives enhance the sinterability of $BaSnO_3$-based materials, a preliminary screening was conducted, taking conventional Ba-based proton-conducting perovskites into consideration.

Table 1 shows some literature data on the relative density of $BaCeO_3$-, $BaZrO_3$-, and $Ba(Ce,Zr)O_3$-based materials prepared without and with the addition of sintering additives. These data indicate that CoO_x, NiO, CuO, and ZnO are the most effective sintering additives for the preparation of highly dense ceramics at reduced

temperatures. In particular, the sintering temperatures can be reduced to 1400–1450 °C, which is suitable for the fabrication of not only individual ceramic materials but also thin films of multilayered electrochemical cells.

Despite many promising results, the comparison of these results is often a challenging endeavor. First, some authors compared the microstructural parameters of ceramics (and their other functional properties) using the same synthesis and sintering regimes. In this case, the porous samples were obviously obtained without sintering additives. In contrast, other authors sought to eliminate the effect of density/porosity, providing a comparative analysis between ceramic samples with comparable relative densities. This means that the ceramics without sintering additives were prepared at much higher sintering temperatures than those with sintering additives. Second, sintering additives are employed in a variety of forms. Some researchers utilized them as dopants, providing a partial substitution of basic cations with 3d-elements, whereas other researchers incorporated them as a secondary phase, using terms of weight or volume fraction ratios.

Table 1. Relative density (ρ) and average grain size (D) of the proton-conducting ceramics obtained with the addition of sintering additives.

Composition [a]	x	x (wt%)	Synthesis route	T_{syn} (°C)	T_{sin} (°C)	ρ (%)	D (μm)	Ref.
BCG	–	–	ultrasonic-assisted precipitation	1000	1450	69	6.0	[34]
BCG + x wt.% NiO	0.5	0.5				82	–	
	1	1				95	11.7	
	1.5	1.5				97	22.8	
BCG + x wt.% Co_2O_3	0.5	0.5				89	–	
	1	1				95	–	
	1.5	1.5				97	14.0	
BCG + x wt.% ZnO	0.5	0.5				85	–	
	1	1				88	12.0	
	1.5	1.5				82	–	
BCZYY	–	–	solid-state synthesis	1150	1450	85	2.3	[35]
BCZYYb + x wt.% NiO	1	1				96	15.3	
BCZYYb + x wt.% CuO	1	1				98	18.2	
BCZYYb + x wt.% ZnO	1	1				85	4.4	
BZY	–	–	solid-state synthesis	1300	1670	94.2	0.15	[36]
BZY + x mol.% CuO	1	0.27		1300	1450	95.8	0.05	
BZY + x mol.% NiO	1	0.25				90.6	0.06	
BZY + x mol.% ZnO	1	0.27				91.9	0.05	
BZY + x mol.% SnO	1	0.45				83	–	
BZY + x mol.% MgO	1	0.13				86	–	
BZY + x mol.% Al_2O_3	1	0.34				88.6	–	
BCZY	–	–	citrate-nitrate combustion synthesis	1100	1600	98	–	[37]
BCZY	–	–		1100	1400	87	–	
BCZY + x wt.% CuO	1	1				96	–	
BCZY + x wt.% NiO	1	1				97	–	
BCZY + x wt.% ZnO	1	1				98	–	
BCG	–	–	freeze-dried precursor preparation	1000	1400	100	1.2	[38]
BCG + x wt.% CoO_n	2	0.46		1000	1200	100	1.1	
BCG + x mol.% ZnO	0.5	0.12				93	0.5	

	2	0.50				99	1.2	
	5	1.24				97	1.5	
BCG + x mol.% NiO	2	0.46				90	0.5	
BCG + x mol.% CuO	2	0.50				98	1.1	
BZY	–	–	solid-state synthesis	1300	1700	97	1.05	[39]
BZY + x mol.% CuO	1	0.27		1300	1500	97	1.24	
BZY + x mol.% ZnO	4	1.09		1250	1300	97	0.67	
BCZY0.6	–	–	solid-state synthesis	-	1650	–	1.3	[40]
BCZY631 + x mol.% CuO	5	1.30			1450	95	6.2	
BCZY631+ x mol.% ZnO	5	1.30			1450	95	–	
BCZY631 + x mol.% Fe_2O_3	5	2.54			1600	90	3.3	
BCZY631 + x mol.% PdO	5	1.95			1600	90	1.4	
BCZY631 + x mol.% Cr_2O_3	5	2.42			1600	90	0.35	
BCZYYb442	–	–	spray pyrolysis	–	1650	91	6.3	[26]
BCZYYb442 + x wt.%NiO	0.5	0.5				97	23.9	
	1	1				99	38	
	2	2				99	56.4	
BCZYYb442 + x wt.%ZnO	0.5	0.5				95	15.1	
	1	1				97	21.2	
	2	2				98	35.1	
BCZYYb442 + x wt.%CuO	0.5	0.5				96	13.9	
	1	1				98	25.6	
	2	2				99	31.1	
BCZY442	–	–	solid-state synthesis	–	1600	71	19.7	
BCZY442 + x wt.% NiO	0.5	0.5				98	40.3	
	1	1				99	43.7	
BCZY442 + x wt.% CuO	0.5	0.5				96	21.9	
	1	1				98	37.4	
BCG	–	–	solid-state synthesis	1100	1450	86	0.8	[41]
BCG + x mol.% CuO	1	0.25				91	3.4	
BCG + x mol.% Co_3O_4	1	0.74				94	6.9	
BCG + x mol.% NiO	1	0.23				97	9.6	
$BCZYCo_x$	0.02	0.52	modified Pechini	1000	1425	>95	1.5	[42]
	0.03	0.77					1.05	
	0.05	1.29			1300		0.62	
	0.1	2.60			1100		0.32	
$BZYCo_x$	0	0.00	solid-state synthesis	1400	1450	79.2	0.05−0.3	[43]
	0.01	0.27				94.9		
	0.02	0.53				95		
	0.05	1.34				95.1		
$BCZY72Co_x$	0.01	0.26				96.3	0.3−0.5	
	0.02	0.53				97.1		
	0.05	1.32				93.9		
$BZYNi_x$	0.01	0.25				91.9	0.2−1	
	0.02	0.50				94.2		
$BCZYNi_x$	0.01	0.24				94.4	0.5−1	
	0.02	0.49				94.4		
$BCGCo_x$	0	0.00	solid-state synthesis	1150	1450	81	2	[44]
	0.01	0.25				96	3−7	
	0.03	0.74				97	>10	
	0.05	1.24				96		
	0.07	1.75				96		
	0.1	2.52				94		

[a] **Electrolyte composition abbreviations**: BCG = $BaCe_{0.9}Gd_{0.1}O_{3-\delta}$, BCZYYb = $BaCe_{0.7}Zr_{0.1}Y_{0.1}Yb_{0.1}O_{3-\delta}$, BZY = $BaZr_{0.85}Y_{0.15}O_{3-\delta}$, BCZY = $BaCe_{0.3}Zr_{0.55}Y_{0.15}O_{3-\delta}$, BCZY631 = $BaCe_{0.6}Zr_{0.3}Y_{0.1}O_{3-\delta}$, BCZYYb442 = $BaZr_{0.4}Ce_{0.4}(Y,Yb)_{0.2}O_{3-\delta}$, BCZY442 = $BaZr_{0.4}Ce_{0.4}Y_{0.2}O_{3-\delta}$, $BCZYCo_x$ = $BaCe_{0.5}Zr_{0.4}Y_{0.1-x}Co_xO_{3-\delta}$, $BZYCo_x$ = $BaZr_{0.9}Y_{0.1-x}Co_xO_{3-\delta}$, $BCZY72Co_x$ = $BaZr_{0.7}Ce_{0.2}Y_{0.1-x}Co_xO_{3-\delta}$, $BZYNi_x$ = $BaZr_{0.9}Y_{0.1-x}Ni_xO_{3-\delta}$, $BCZYNi_x$ = $BaZr_{0.7}Ce_{0.2}Y_{0.1-x}Ni_xO_{3-\delta}$, $BCGCo_x$ = $BaCe_{0.9-x}Gd_{0.1}Co_xO_{3-\delta}$.

Following this analysis, the $BaSn_{0.8}Y_{0.2}O_{3-\delta}$ ceramic samples were prepared with the incorporation of 1 wt% Co_3O_4, NiO, and CuO as sintering additives, with a sintering temperature of 1500 °C being necessary to ensure the maintenance of the single-phase state. **Figure 3** shows the resulting XRD patterns for the $BaSn_{0.8}Y_{0.2}O_{3-\delta}$ ceramic samples prepared in this way. These spectra are in close agreement with the ICDD

PDF-2 card for Y-doped $BaSnO_3$. All the samples were found to be single phase and crystallized into a cubic perovskite structure, exhibiting no evidence of secondary phases associated with sintering additives. The lattice parameters of the pristine and modified samples fall within a range of 4.168±0.005 Å, remaining virtually unchanged due to the low concentration of the introduced impurities. While the phase state of the modified stannates is identical to that of the pristine barium stannate, the relative density of the Co, Ni-, and Cu-containing samples increased considerably, from 60% to 96%, 97%, and 98%, respectively. This suggests that the introduced sintering additives effectively enhance the densification of $BaSnO_3$ as a representative Ba-containing perovskite oxide (**Table 1**).

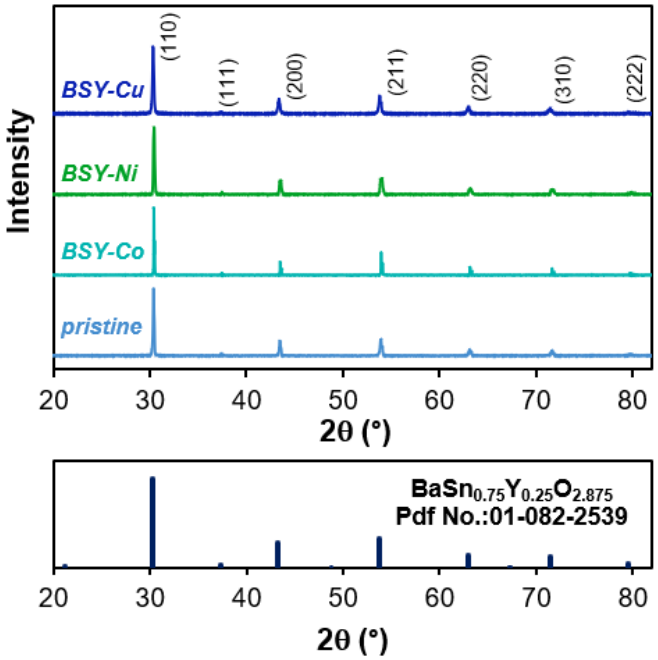

Figure 3. XRD patterns of the $BaSn_{0.8}Y_{0.2}O_{3-\delta}$ pellets calcined at 1500 °C in ambient air and the corresponding ICDD PDF-2 card for Y-doped $BaSnO_3$.

The enhanced sinterability of ceramic materials in the presence of sintering additives is typically attributed to the formation of low-melting phases, i.e., through liquid phase sintering [21,45,46]. In summary, a solid system is subjected to a heating process until its constituent components are melted. The appearance of the liquid phase led to wetting of the grains. This changes the mass diffusion mechanism, from limited solid–solid paths to solid–wet paths, facilitating grain rearrangement, grain coarsening, and densification. A source of possible liquid phases is either individually introduced

3d oxides (for example, ZnO or Cu_2O), their low-melting binary oxides (for example, $BaZnO_2$ or $BaCuO_2$), or low-melting eutectics (for example, $BaNiO_2$–Ba_3NiO_4); the melting point of these substances ranges from 900 to 1200 °C, depending on the type of 3d element and its concentration [21,28,47]. Importantly, during the cooling process, low-melting phases should preferably be localized at the grain boundaries of the ceramics because of capillary forces. However, these impurities are often difficult to detect at the micron (or even submicron) level; thus, their influence is usually monitored by indirect signs, such as reduced dehydration, a lower protonic conductivity level, etc. To elucidate the similarities and differences between the utilized sintering additives, the microstructural characteristics of the prepared ceramics were examined and analysed in the next sections.

3.2. Microstructural analysis of the prepared ceramics

Figure 4a shows the SEM images obtained for a surface (untreated) region of the ceramic materials at 1500 °C. As can be seen, all three samples exhibited dense packing of grains and a negligible presence of pores, confirming facilitated densification upon the introduction of the studied sintering additives. Despite the good quality of the ceramics, microstructural analysis is better for obtaining polished sections, which act as the bulk sign of ceramics. In other words, the shape and size of surface and bulk grains may exhibit notable discrepancies. This discrepancy can be attributed to the different densification kinetics of the internal grains compared with those of the surface grains, as confirmed in our previous works [48,49]. Indeed, as shown in **Figure 4b**, the grains were well formed and densely packed for all the studied ceramics. However, some volume defects (see an example for the Cocontaining sample) and the presence of impurity phase(s) (see an example for the Ni-containing sample) can also be observed. The microstructural parameters of the Cu-containing sample were found to be the best, although some close pores were also identified in the enlarged SEM image (**Figure 5a**). Among the three samples, the Cocontaining sample exhibited the greatest amount of grain growth, with an average grain size of ~2.5 μm, whereas only 1.7 μm growth was achieved for the Cu-containing sample (**Figure 4c**).

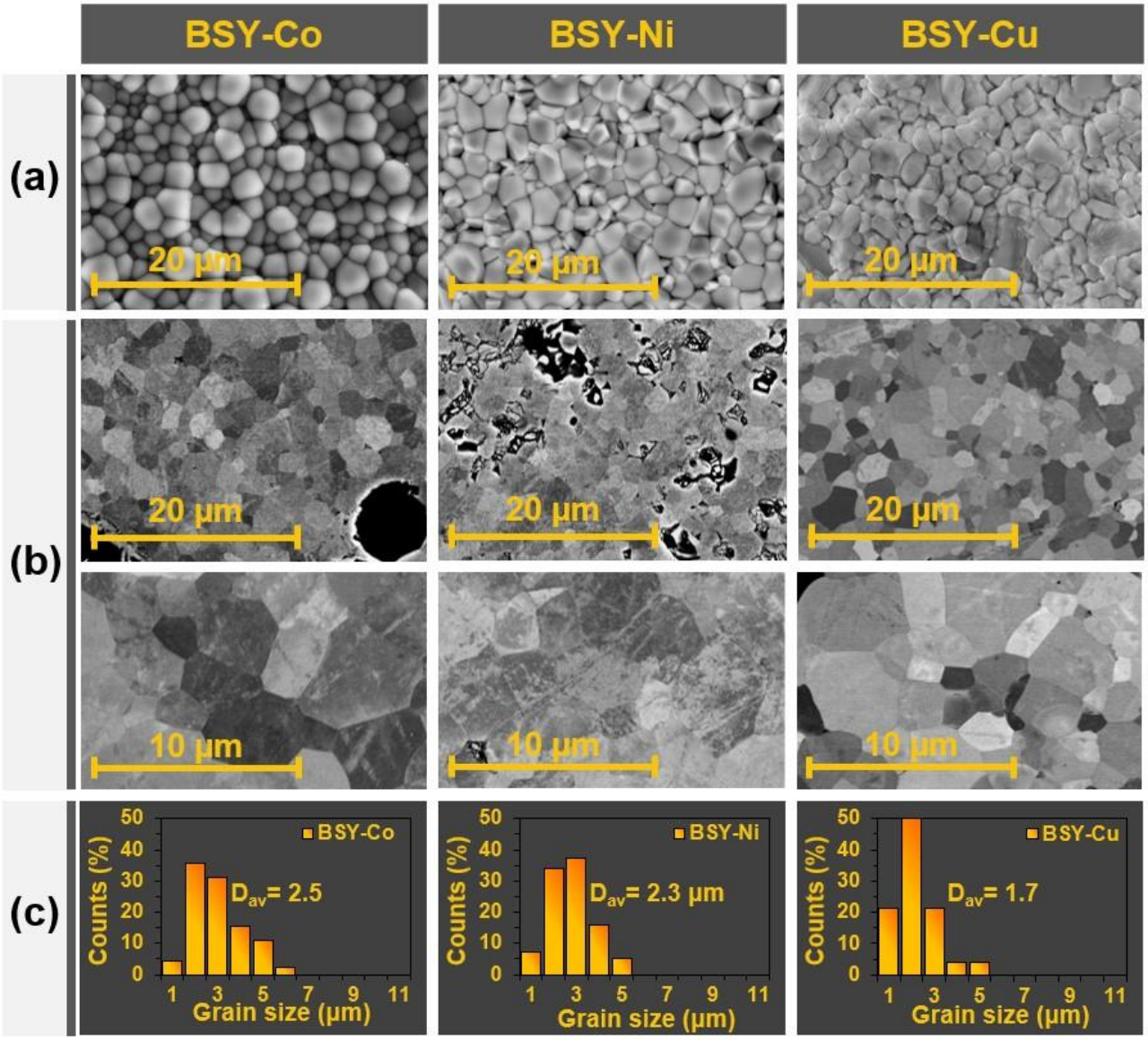

Figure 4. Scanning electron microscopy data for the dense $BaSn_{0.8}Y_{0.2}O_{3-\delta}$ + 1 wt% MO_x ceramic samples: (a) SEM images of the as-prepared samples, (b) SEM images of the polished samples, and (c) grain size distribution analysis of the polished sections.

To provide a comprehensive chemical composition assessment, EDX spectroscopy was employed for both local and integral chemical analysis of the polished ceramic sections (**Figure 5)**. The results revealed that the three samples exhibited markedly distinct features with respect to the localization and concentration of the introduced sintering additives.

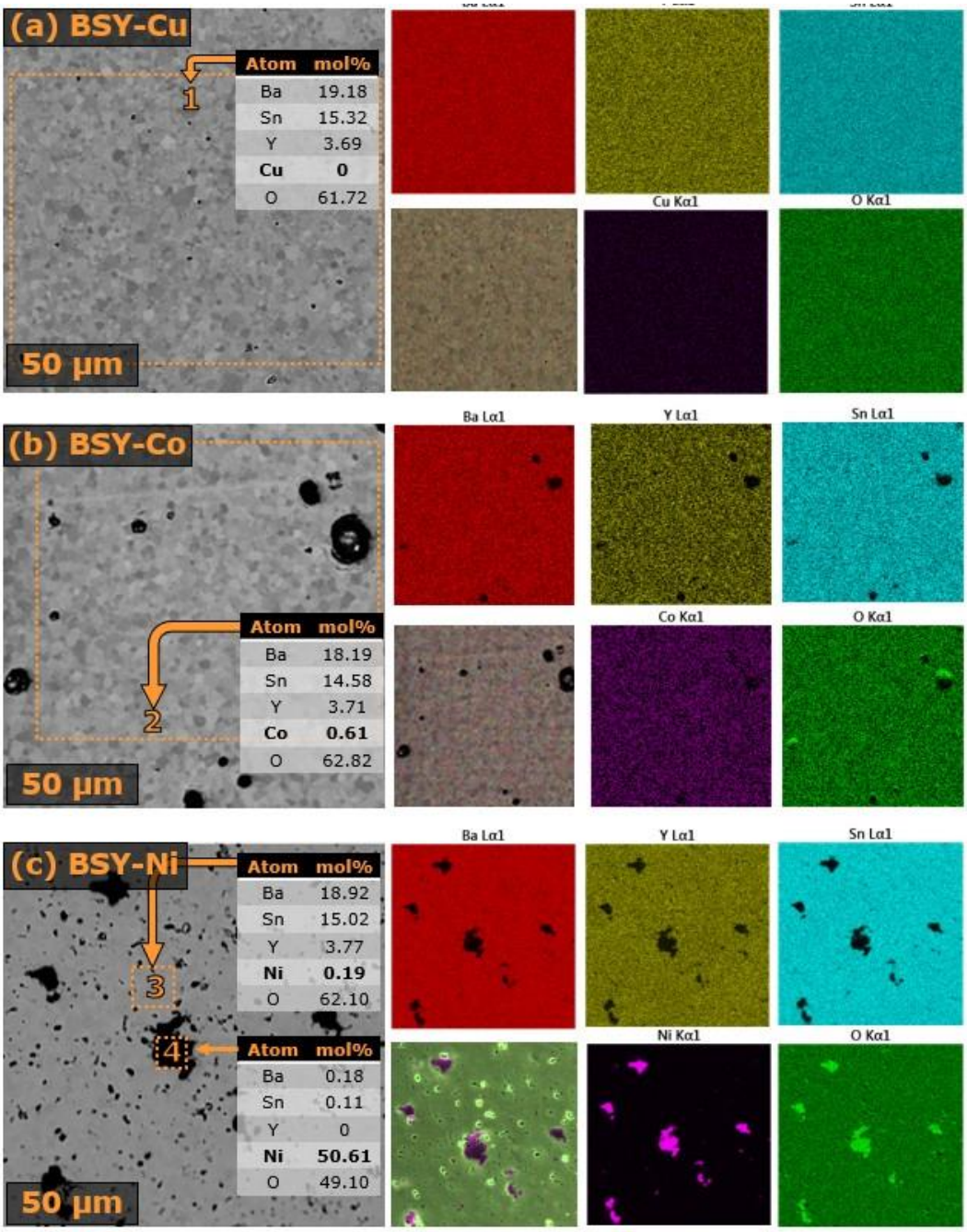

Figure 5. SEM image of the polished $BaSn_{0.8}Y_{0.2}O_{3-\delta}$ + 1 wt% MO_x ceramic samples and corresponding EDX analysis: (a) M = Cu, (b) M = Co, and (c) M = Ni.

For the Cu-containing ceramic sample (**Figure 5a**), a very low number of volume defects (close pores with a diameter of several microns) can be observed. The element distribution maps exhibited high homogeneity with respect to all basic cations, indicating the absence of local regions related to secondary phases. However, the average chemical analysis performed for a region marked by Frame 1 (**Figure 5a**) revealed no detectable Cu concentration within the volume of the ceramic body. This

finding is surprising given that 1 wt% CuO should be detected principally via EDX analysis.

In the case of the Cocontaining ceramic sample (**Figure 5b**), the primary perovskite elements and Co ions were observed to be distributed in a uniform manner across the polished section. This material exhibited quite large pores, which were observed to be locally formed. The EDX analysis (within Frame 2) revealed the presence of cobalt in this section, with a concentration of ~0.6 mol% (or ~3.1 mol% after cationic normalization). The nominal mole concentration of CoO_x in the $BaSn_{0.8}Y_{0.2}O_{3-\delta}$ + 1 wt% CoO_x ceramic is approximately 3.5 mol%. This finding indicates that only 88% of the total cobalt introduced was detected via EDX analysis.

The backscattering electron mode for the Ni-containing sample (**Figure 5c**) reveals the presence of dark segments with varying dimensions and shapes. The small rounded segments with a diameter of 1–5 μm were identified as pores, whereas the large segments were attributed to a Ni-enriched phase. A more precise EDX analysis (Frame 4) indicates that this impurity is composed of almost pure NiO due to zero solutions for the Ba, Y and Sn distribution maps. Additionally, trace amounts of Ni ions (~0.2 mol%) were detected in the grain region of the ceramic (Frame 3), indicating that approximately 20% of the initially introduced NiO was dissolved within the perovskite structure.

Several interesting conclusions can be drawn from the obtained experimental results.

The first specific case pertains to the Ni-containing sample. The incorporation of NiO results in its segregation as discrete and sizable inclusions within the volume of the main perovskite phase. The analysis of Ni-containing ceramics of Ce- or Zr-based perovskites also revealed the formation of a Ni-rich phase as large inclusions (see the supplementary materials, **Figure S1** [25,26,34,50,51]) instead of its expected distribution along grain boundaries in the liquid phase sintering process. This observation suggests that the solubility of Ni cations in the Ce-, Zr-, or Sn-subltices of Ba-based perovskites is extremely low, although it is evidently sufficient to increase material densification.

Second, the nature of the Ni-based impurities in sintered ceramics of various families differs. In numerous reports, BaY_2NiO_5 was proposed to be formed upon the addition of NiO to Y-doped $BaZrO_3$ or $BaCeO_3$ ceramics [25,50,52]. The $BaSn_{0.8}Y_{0.2}O_{3-\delta}$ composition also comprises the Ba- and Y-elements required for the formation of BaY_2NiO_5, yet only the NiO phase was identified as an impurity. Consequently, more insights are necessary to ascertain the origin and conditions governing the formation of both BaY_2NiO_5 and NiO impurities.

Finally, the detectable concentrations of CuO and CoO_x sintering additives were found to be lower than their nominal contents when the polished sections of the corresponding ceramics were examined. Moreover, the experimental concentrations of other cations are in close agreement with the nominal values (**Figure 6a**). Although the EDX detection errors can be quite high for relatively light elements with low concentrations, this still cannot explain the near-zero concentration for CuO. To verify the EDX data, chemical analysis with inductively coupled plasma–mass spectrometry was used to determine the actual concentrations of copper, cobalt, and nickel oxides. As shown in **Figure 6b**, their real concentrations are indeed lower than the introduced values: approximately 0.13, 0.72, and 0.88 wt% for CuO, CoO_x, and NiO, respectively. Again, 0 and 0.88 wt% were found for CuO and CoO_x, respectively, according to the EDX analysis. Therefore, both approaches indicate that the CuO concentration for the Cu-containing stannate is approximately 90% less than the nominal value.

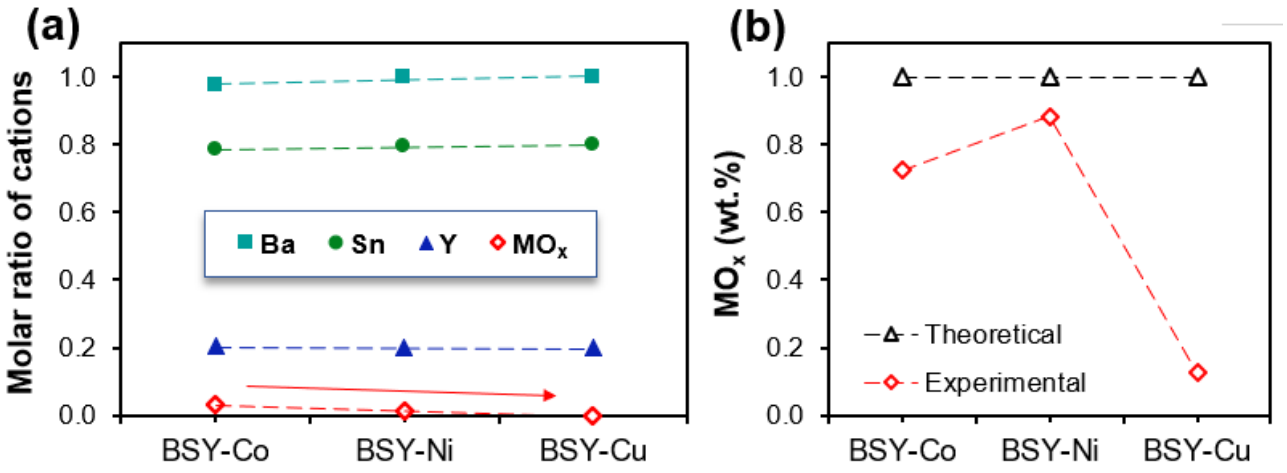

Figure 6. Molar ratio of cations and sintering additive concentration for $BaSn_{0.8}Y_{0.2}O_{3-\delta}$ + 1 wt% MO_x calculated from (a) energy-dispersive spectroscopy and (b) inductively coupled plasma–mass spectrometry.

The reduced concentration of sintering additives in the prepared ceramics can be explained by considering the corresponding phase diagrams. Since low-melting components appear for a wide range of Ba-containing perovskites, the $BaO–MO_x$ phase diagrams can be rationally analysed. The fragments of these diagrams are presented in **Figure S2**.

A BaO–CuO phase diagram includes the existence of several low-melting compounds (Ba_2CuO_3, $BaCuO_2$, $Ba_2Cu_3O_5$), several phase decomposition regions ($BaO_2 \rightarrow BaO$, $CuO \rightarrow Cu_2O$) and high-temperature phase transitions, as shown in **Figure S2a** [53]. Of particular interest is the observation that the eutectic temperatures for this phase diagram are relatively low (890–920 °C) for all the component ratios.

Figure S2b presents a fragmentary BaO–NiO phase diagram [54]. This illustrates the existence of two $BaNiO_2$ and Ba_3NiO_4 compounds, which form a common eutectic with a liquid phase that appears at approximately 1080 °C.

The Ba–Co–O phase diagram is seemingly the most complicated because of the complex nature of the intermediates ($BaCoO_3$, Ba_2CoO_4) that can be formed in this system. No $BaO–CoO_x$ phase diagram was found from the available sources, although some isothermal fragments were reported for triangle phase diagrams (**Figure S2c)**. According to these data, a liquid phase appears at 1100 °C in the cobalt-rich region of the $BaO–CoO_x$ phase diagram [55].

A comparison of the results reveals that the eutectic temperatures in the Ba–Cu–O system are significantly lower temperatures (by 150–200 °C) than those observed for the Ba–Ni–O and Ba–Co–O systems. This suggests that the volatility (evaporation) temperatures of the Cu-based compounds are also lower than those of the Ni- and Cobased compounds. This may provide an explanation for the extremely low concentration of CuO in the ceramic sintered at 1500 °C in comparison to the nominal concentration, indicating that a significant portion of the CuO evaporated. In contrast, only a minor quantity of cobalt- and nickel-based oxides underwent evaporation under the same sintering conditions.

It is important to note that a single microstructural analysis of the obtained samples is insufficient for a more precise estimation of the sintering additive localization. This is because the concentration of the introduced impurity may be insufficient for equipment resolution. Consequently, we further investigated the microstructure of the samples after their reduction in a hydrogen atmosphere.

3.3. Microstructural analysis of the reduced ceramics

After SEM and EDX analyses, the polished ceramic samples were then treated in a wet hydrogen atmosphere (3% H2O/H_2) at 700 °C for 10 h. This treatment is expected to initiate an exsolution process of Co, Ni, and Cu ions upon the release of metallic particles due to the high redox activity of 3d-elements. The reduced samples were subsequently analysed in the same manner as their pretreated ceramics.

Figure 7 shows the results of the microstructural analysis for all the studied materials containing sintering additives. These samples again demonstrate individual chemical features related to the exsolution of 3d-elements. Considering the Cocontaining sample (**Figure 7a**), no visible Cobased sediments were identified across the entirety of the surface. Moreover, the results of qualitative chemical analysis (see mole percentage values) of the oxidized and reduced ceramics are almost the same, taking measurement errors into account. This could indicate that the Co ions are fully dissolved in the perovskite structure and that the provided reduction force is insufficient to exsolve these ions from the structure. Indeed, the literature analysis has shown that cobalt can be incorporated into cerates or zirconates in significant quantities, exceeding x = 0.05 (up to x = 0.15) for $BaM_{1-x}Co_xO_{3-\delta}$ (M = Ce, Zr, or Ce/Zr), depending on the basic phase composition and sintering conditions [42,44,56–59]. In turn, these mole ratios exceed 1 wt%, as utilized in the present work.

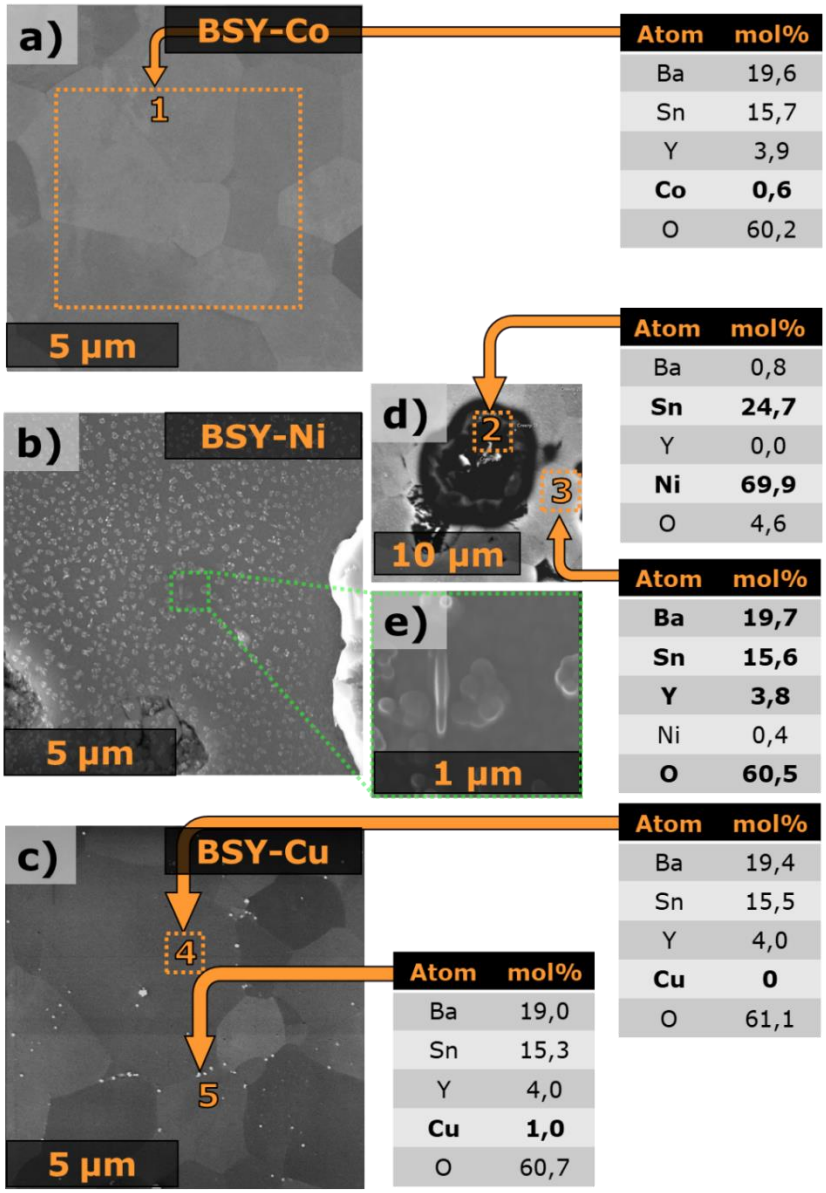

Figure 7. SEM images of polished $BaSn_{0.8}Y_{0.2}O_{3-\delta}$ + 1 wt% MO_x pellets reduced in wet H_2 (pH_2O = 0.03) at 700 °C for 10 h: (a) M = Co, (b) M = Ni, (c) M = Cu. Some defects in the Ni-containing ceramic are also shown in panels (d) and (e).

Unexpected results were obtained for the Ni-containing sample (**Figure 7b)**. It can be postulated that NiO, which was detected in the oxidized ceramic, should undergo its reduction until a metallic form is reached, namely, pure nickel. However, the EDX analysis indicated that the reduced particles contained a considerable amount of tin. The approximate molar ratio of Ni:Sn was determined to be 3:1 (**Figure 7d**), which corresponds to Ni_3Sn. This intermetallic compound indeed exists; see the Ni-enriched region of the corresponding Ni–Sn phase diagram (**Figure S3** [60,61]). It is likely that a portion of the Sn ions from the ceramic surface were reduced in wet

hydrogen, resulting in the formation of a liquid phase (as evidenced by the Sn-enriched boundary of the phase diagram at 700 °C). The wettability of the oxide phase by this liquid is clearly inferior to that of the metallic phase. Consequently, the liquid tin tends to interact with the reduced Ni phase, forming an almost stoichiometric Ni_3Sn intermetallic alloy. This may be the reason why the EDX analysis indicated the formation of Ni_3Sn instead of pure nickel. As a consequence of the slight depletion of the surface region by tin ($BaSn_{0.8-\alpha}Y_{0.2}O_{3-\delta}$), this region becomes enriched by barium in accordance with the B-position normalization: $BaSn_{0.8-\alpha}Y_{0.2}O_{3-\delta} \equiv Ba_{1/(1-\alpha)}(Sn_{0.8-\alpha}Y_{0.2})_{1/(1-\alpha)}O_{3-\delta}$. Ba-overstoichiometric (or Ba-excess) compounds are known to be more capable of carbonization than their stoichiometric or Ba-deficient counterparts [62–64]. It can be reasonably postulated that such carbonate formation may occur naturally during the contact of reduced samples with air even at room temperature, i.e., after high-temperature reduction experiments and before microscopic analysis. Consequently, the identified submicron particle populations are attributed to $BaCO_3$ (**Figure 7e**). These particles were observed to cover the entire surface of the Ni-containing ceramic in contrast to the Cu- and Cobased ceramics, whose surface was almost pure.

Figure 7c shows the surface section of the reduced Cu-containing sample. The majority of the exsolved particles were observed at the grain boundaries of the ceramics, with a minor presence within the grains. The particles were observed to be no larger than 100 nm in size (**Figure S4**). The EDX analysis of the bulk grains did not yield any quantifiable amount of copper. However, point analysis of individual nanoparticles indicated the presence of a relatively small quantity of copper. While these qualitative data are insufficient for drawing conclusions about the actual copper content, they confirm that the exsolved phase is enriched by copper.

Importantly, the presence of small amounts of Cu-based phases is challenging to detect via conventional SEM+EDX analysis, particularly for oxidized ceramics. Recently, we employed scanning electron microscopy (SEM) coupled with electron backscatter diffraction (EBSD) to address this challenge [65,66]. Our findings demonstrated that CuO could not be detected via either secondary electron imaging or

backscattered electron mode. However, the application of EBSD enabled the detection of the CuO phase (**Figure S5**). The latter was initially distributed along the grain boundaries, but this distribution was not continuous: some portions of the grain boundaries were free from the CuO nanoparticles, whereas other grain boundaries were partially or completely covered by these nanoparticles. These observations showed that the CuO introduced during the sintering process prefers to reach the grain boundaries of the ceramics; this fact was confirmed by the EBSD method in the case of the oxidized ceramics and by the SEM+EDX method in the case of the reduced ceramics.

3.4. Effect of sintering additives on the transport of $BaSn_{0.8}Y_{0.2}O_{3-\delta}$ ceramics

Ceramic materials with high relative density (i.e., those containing sintering additives) were subjected to comparative analysis via the EIS technique. The obtained spectra were analysed according to the widely accepted model (**Figure 8a**), which includes ionic transport stages associated with bulk transport in polycrystalline materials, grain boundary transport and interface- and electrode-related processes [67–69]. The latter were significant at low temperatures, whereas only electrolyte-related resistances were present in the hodographs at higher temperatures. To describe the partial resistances of the overall EIS spectra, CPE elements with R, Q, and n terms were employed, where R represents the resistance, Q is the double-layer capacitance parameter, and n is the dimensionless CPE exponent. These parameters were then utilized to calculate the characteristic capacitance and frequency values as follows: $C_i = (R_i \cdot Q_i)^{1/n_i} \cdot R_i^{-1}$ and $f_{max,i} = (R_i \cdot Q_i)^{-1/n_i} \cdot (2\pi)^{-1}$. **Figure 8b–d** shows examples of the provided fitting, whereas **Figure S6** presents the temperature dependences of the capacitances and frequencies, whose absolute values (along with their temperature variation) indicate a comparable nature of the processes attributed to the first and second semicircles of the EIS hodographs for all three studied ceramic materials.

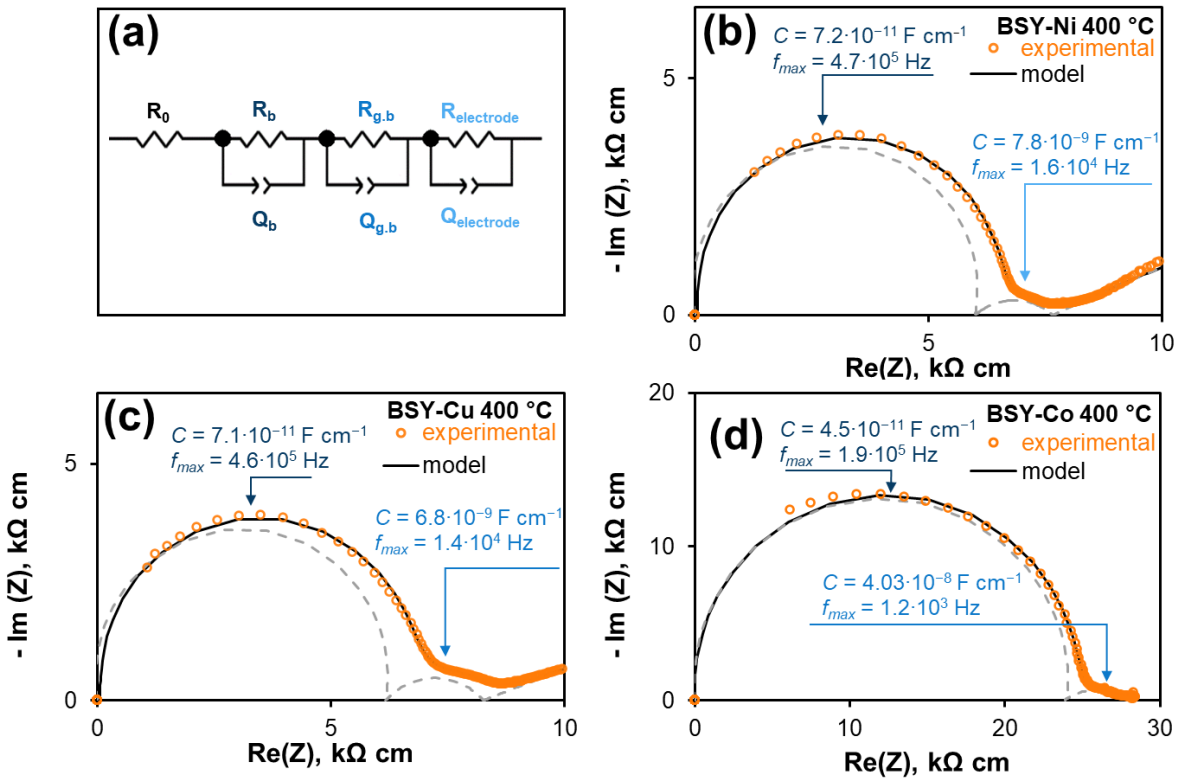

Figure 8. EIS analysis of the $BaSn_{0.8}Y_{0.2}O_{3-\delta}$ + 1 wt% MO_x ceramic materials in wet air: (a) Equivalent circuit scheme, the examples of the provided fitting for M = Ni (b), M = Cu (c), and M = Co (d).

Figure 9 shows that the temperature dependence of the Co, Ni-, and Cu-containing ceramic samples is linear, albeit with different activation energy (Ea) values. First, a comparison of the total conductivities in **Figure 9b** reveals that the Ni- and Cu-containing samples exhibited similar conductivities and Ea values. In contrast, the total conductivity of the Cocontaining sample was considerably lower, reaching approximately one order of magnitude at 250 °C. To identify the underlying causes of these observations, a comparative analysis of both bulk and grain boundary conductivities was further conducted. According to **Figure 9c**, the bulk conductivity of the Cobased ceramic sample was also lower than those of its Ni- and Cu-based counterparts. The bulk transport should not be affected by the microstructural parameters in the case of ceramics with the same nominal composition. Therefore, we propose that the introduced cobalt oxide was dissolved in barium stannate, forming a common solid solution during the high-temperature sintering stage. In contrast, the other sintering additives did not dissolve to a significant extent and thereby did not

significantly affect the bulk properties of the materials. This assumption is also confirmed by the calculated Ea values when the Cobased sample exhibited an Ea value of ~0.7 eV, which is 0.15–0.2 eV greater than those observed for the other two samples. More precisely, 0.5 eV for the bulk conductivity is a characteristic indicator of proton-conducting materials [70], while its increase may suggest a decrease in proton transport and the potential onset of oxygen-ionic conduction. **Figure 9d** shows that the Ni-containing sample has the highest grain boundary conductivity, which can be attributed to the relative purity of the grain boundaries in the oxidized Ni-containing ceramic. The grain boundary conductivity of the Cu-containing sample was lower as a result of the localization of the Cu-based phases at the grain boundaries, as observed in the reduced ceramic. The Cocontaining sample presented the lowest grain boundary conductivity values, despite having a relatively favourable microstructure. This observation can be attributed to the fact that the Cobased sample displays a distinct transport behavior (discussed above in the context of bulk properties), which consequently causes the grain boundary transport differences between the Co and Ni-/Cu-containing ceramic materials.

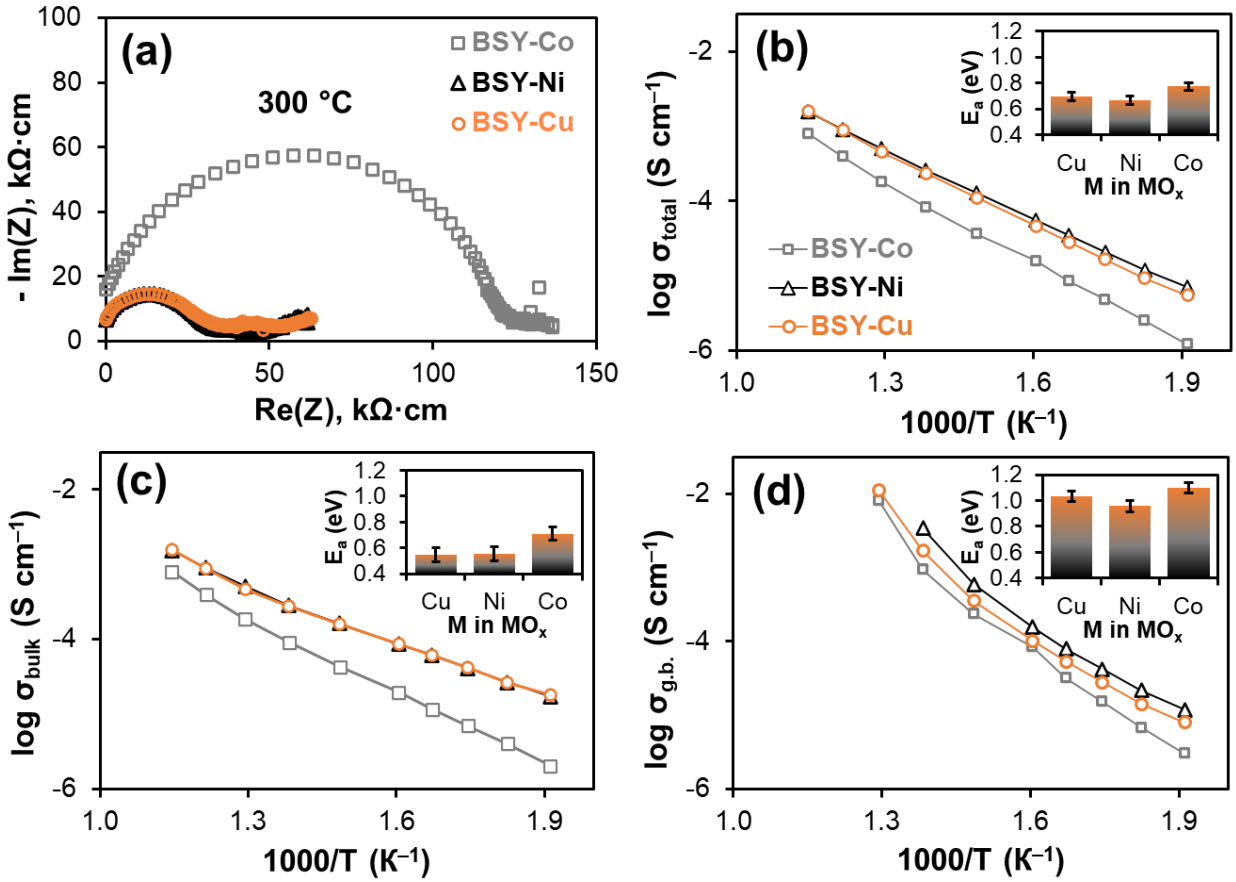

Figure 9. EIS data for the $BaSn_{0.8}Y_{0.2}O_{3-\delta}$ + 1 wt% MO_x ceramic materials in a wet air atmosphere (pH_2O = 0.03 atm, pO_2 = 0.21 atm): (a) comparison of the impedance spectra for the materials at 300 °C, (b) temperature dependences of the total conductivity, (c) temperature dependences of the bulk conductivity, and (d) temperature dependences of the grain boundary conductivity.

3.5. Linking the microstructural and transport properties of $BaSn_{0.8}Y_{0.2}O_{3-\delta}$-based ceramics

In light of the experimental details obtained in **Sections 3.2–3.4**, suggestions can be formulated regarding the localization of Co, Ni-, and Cu-based sintering additives in the sintered $BaSn_{0.8}Y_{0.2}O_{3-\delta}$ ceramics.

The introduced Co_3O_4 additive was observed to dissolve in the perovskite structure (**Figures 5b** and **7a**), as no phase segregation or exsolved phase was identified in either the oxidized or the reduced ceramics. In the case of 1 wt% Co_3O_4, the corresponding mole fraction is equal to 3.5 mol%. However, only approximately 3 mol% was found in the bulk of the Cocontaining ceramic, as determined by EDX and inductively coupled plasma–mass spectrometry analyses (**Figures 5b** and **6**). Despite the potential evaporation of a minor quantity of the introduced CoO_x at elevated sintering temperatures, another portion can be incorporated into the Sn site of barium stannate: $BaSn_{0.8}Y_{0.2}Co_{0.03}O_{3-\delta}$. Considering analogous systems, such as $BaCeO_3$ and $BaZrO_3$ [43,44,38,71], cobalt introduction results in a notable decline in ionic conductivity relative to that of Co-free ceramic samples. In addition, the lowest conductivity was observed for the $BaCe_{0.9}Gd_{0.1}O_{3-\delta}$ ceramic prepared with 2 mol% cobalt oxide; at the same time, the ionic conductivities of the $BaCe_{0.9}Gd_{0.1}O_{3-\delta}$ ceramics with 2 mol% copper, zinc, and nickel oxides were somewhat higher, thereby corroborating the present results (**Figures 8** and **9**).

The provided analysis indicates that CoO_x affects the microstructural and transport properties of Ba-based perovskites in a similar manner. The deterioration in ionic conductivity upon the addition of CoO_x may be attributed to the differing transition oxidation states of cobalt and the tendency of Co ions to adopt a 6-coordinated environment. These factors result in a reduction in the concentration and mobility of proton defects as well as an increase in p-type electronic charge carriers.

As a result, despite the significant enhancement in microstructural properties, it is not feasible to categorize CoO_x as a suitable sintering additive for a diverse range of Ba-based perovskites.

In the case of the Ni-containing $BaSn_{0.8}Y_{0.2}O_{3-\delta}$ ceramic, the formation of substantial NiO sediments was observed following the addition of NiO during the material sintering process (**Figure 5c**). However, these sediments were observed to be isolated from one another, thereby enabling ionic transport through free grain boundaries and grains. Furthermore, the EDX chemical analysis indicates that approximately 20% of the introduced NiO can be dissolved in the perovskite phase, which is 4.5 times lower than the dissolution of CoO_x. This may be the reason why the Ni-containing sample exhibited a higher bulk conductivity than the Co-containing one (**Figure 9**). The high-temperature reduction of the polished Ni-based ceramic did not reveal any particle formation at the grain boundaries (**Figure 7b, d, e**), indicating that a liquid phase that emerged during the sintering process can be dissolved in the perovskite structure during cooling, resulting in no detectable segregation at the grain boundaries. This phenomenon may account for the observation that the Ni-containing ceramic exhibited the highest grain boundary conductivity among all the considered samples. However, Ni-based ceramics exhibit poor chemical stability in reducing environments, which prevents their real high-temperature application in H_2-containing environments.

For the Cu-containing sample, a detectable amount of CuO was found to be ~10% of the nominal introduced value (**Figures 5a**, **6**, and **7c**) when the stannated samples were sintered at 1500 °C to achieve their single-phase form. As a result, a major portion of CuO can be evaporated. Another portion of CuO is located at the grain boundaries of the ceramic, as confirmed by the SEM observations of the reduced samples (**Figure 7c**). These aspects might explain why the Cu-based ceramic is characterized by a high bulk ionic conductivity (**Figure 9**) but a lower grain boundary conductivity than the Ni-based ceramic (**Figure 9**).

For the Cu-containing sample, a detectable amount of CuO was found to be ~10% of the nominal introduced value (**Figures 5a**, **6**, and **7c**) when the stannated samples

were sintered at 1500 °C to achieve their single-phase form. As a result, a large portion of the CuO can be readily evaporated. Another part of the CuO is located at the grain boundaries of the ceramic, as confirmed by the SEM observations of the reduced samples (**Figure 7c**). These features may explain why the Cu-based ceramic is characterized by a high bulk ionic conductivity (**Figure 9**) but a lower grain boundary conductivity than the Ni-based ceramic (**Figure 9**).

All these aspects are summarized in **Figure 10**, which provides a schematic representation of the chemical localization features of the various sintering aids employed in the preparation of barium stannate ceramics. A critical analysis of the available sources of sintering additives for $BaCeO_3$-- and $BaZrO_3$-based ceramics reveals features that are evidently common to different Ba-based perovskite oxides.

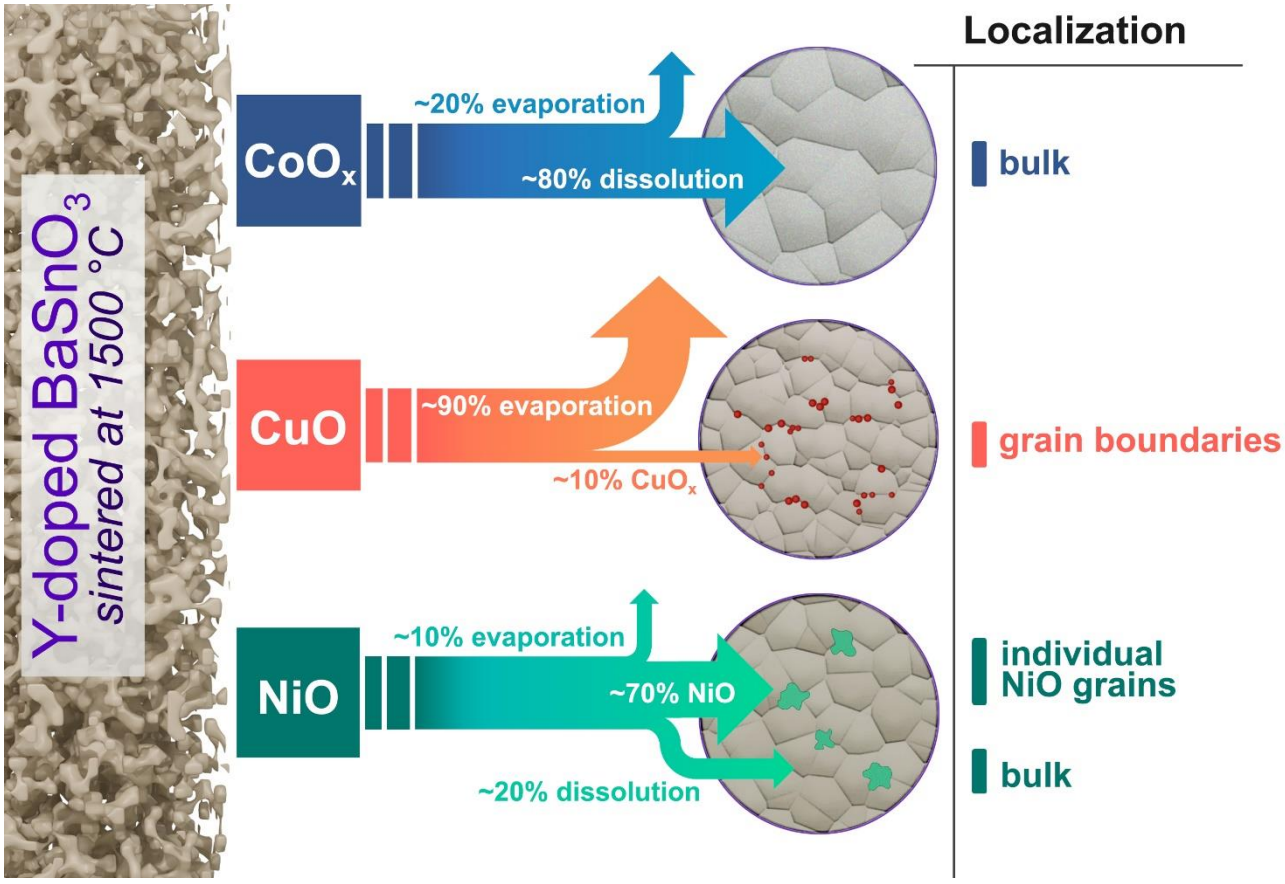

Figure 10. Schematic representation of the localization of different sintering additives in the sintered $BaSn_{0.8}Y_{0.2}O_{3-\delta}$ ceramics.

4. Conclusions

In the present study, three distinct sintering additives (CuO, NiO, and Co_3O_4) were employed for the fabrication of highly dense $BaSnO_3$-based ceramics, which serve as model representatives of proton-conducting materials. $BaSnO_3$ ceramics are very similar to well-known $BaZrO_3$-based ceramics in terms of their poor densification, even when solution techniques are employed. Therefore, the incorporation of sintering additives is considered a highly rational and technologically straightforward approach. The primary objective of this research was to ascertain the potential localization of these additives and their possible impact on the transport properties of the resulting materials. To accomplish this goal, a comprehensive analysis of the microstructure parameters was conducted for both the as-sintered samples and those obtained after their high-temperature reduction in wet H_2 at elevated temperatures.

This research design enables the identification of potential localization sites for the introduced sintering additives in stannate ceramics. Specifically, the introduced Co_3O_4 was fully dissolved in the perovskite structure, which had a detrimental effect on the proton transport of $BaSn_{0.8}Y_{0.2}O_{3-\delta}$. NiO demonstrated limited solubility, forming macroscopic defects (individual NiO grains) within the polycrystalline volume of the ceramic. However, the localized formation of the impurity phase did not significantly impact the bulk or grain boundary transport properties. Ultimately, a significant proportion of CuO (~90%) was lost because of the need for a high sintering temperature (1500 °C) for the formation of single-phase $BaSn_{0.8}Y_{0.2}O_{3-\delta}$ materials. Another portion of CuO was observed to localize at the grain boundaries of the studied ceramic, resulting in a slight decrease in the grain boundary conductivity compared with that of the Ni-containing sample. Nevertheless, CuO was proposed as the most effective sintering additive because of its small concentration in the resulting ceramic.

The provided analysis, in combination with a comparison of the present results with literature data for other proton-conducting materials (cerates and zirconates), allows us to propose a similarity in the ongoing processes and phase relationships upon the introduction of sintering additives. Therefore, this work presents significant

insights into the chemical and electrochemical features of proton-conducting materials containing sintering aids.

Acknowledgements

This work was prepared within the framework of the budgetary plans of the Hydrogen Energy Laboratory (Ural Federal University) and Institute of High-Temperature Electrochemistry (IHTE). The authors thank the "Composition of Compounds" Shared Access Center of IHTE for support in structural and microstructural characterization.

References

[1] B. S. Zainal, P. J. Ker, H. Mohamed, H. C. Ong, I. M. R. Fattah, S. M. A. Rahman, L. D. Nghiem, T. M. I. Mahlia. Recent advancement and assessment of green hydrogen production technologies. Renewable and Sustainable Energy Reviews 189 (2024) 113941. https://doi.org/10.1016/j.rser.2023.113941

[2] N. Ma, W. Zhao, W. Wang, X. Li, H. Zhou. Large scale of green hydrogen storage: opportunities and challenges. International Journal of Hydrogen Energy 50 (2024) 379. https://doi.org/10.1016/j.ijhydene.2023.09.021

[3] S. Sikiru, T. L. Oladosu, T. I. Amosa, J. O. Olutoki, M. N. M. Ansari, K. J. Abioye, Z. U. Rehman, H. Soleimani. Hydrogen-powered horizons: transformative technologies in clean energy generation, distribution, and storage for sustainable innovation. International Journal of Hydrogen Energy 56 (2024) 1152. https://doi.org/10.1016/j.ijhydene.2023.12.186

[4] S. Baratov, E. Filonova, A. Ivanova, M. B. Hanif, M. Irshad, M. Z. Khan, M. Motola, S. Rauf, D. Medvedev. Current and further trajectories in designing functional materials for solid oxide electrochemical cells: A review of other reviews. Journal of Energy Chemistry 94 (2024) 302. https://doi.org/10.1016/j.jechem.2024.02.047

[5] H. Xu, Y. Han, J. Zhu, M. Ni, Z. Yao. Status and progress of metal-supported solid oxide fuel cell: towards large-scale manufactory and practical applications. Energy Reviews 3(1) (2024) 100051. https://doi.org/10.1016/j.enrev.2023.100051

[6] A. Lahrichi, Y. El Issmaeli, S. S. Kalanur, B. G. Pollet. Advancements, strategies, and prospects of solid oxide electrolysis cells (SOECs): towards enhanced performance and large-scale sustainable hydrogen production. Journal of Energy Chemistry 94 (2024) 688. https://doi.org/10.1016/j.jechem.2024.03.020

[7] Y. Wang, J. Shi, X. Gu, O. Deutschmann, Y. Shi, N. Cai. Toward mobility of solid oxide fuel cells. Progress in Energy and Combustion Science 102 (2024) 101141. https://doi.org/10.1016/j.pecs.2023.101141

[8] Y. Xu, S. Cai, B. Chi, Z. Tu. Technological limitations and recent developments in a solid oxide electrolyzer cell: A review. International Journal of Hydrogen Energy 50 (2024) 548. https://doi.org/10.1016/j.ijhydene.2023.08.314

[9] O. Gohar, M. Z. Khan, M. Saleem, O. Chun, Z. U. D. Babar, M. M. U. Rehman, A. Hussain, K. Zheng, J. H. Koh, A. Ghaffar, I. Hussain, E. Filonova, D. Medvedev, M. Motola, M. B. Hanif. Navigating the future of solid oxide fuel cell: comprehensive insights into fuel electrode related degradation mechanisms and mitigation strategies. Advances in Colloid and Interface Science 331 (2024) 103241. https://doi.org/10.1016/j.cis.2024.103241

[10] Y. Wang, W. Li, L. Ma, W. Li, X. Liu. Degradation of solid oxide electrolysis cells: Phenomena, mechanisms, and emerging mitigation strategies—A review. Journal of Materials Science & Technology 55 (2020) 35. https://doi.org/10.1016/j.jmst.2019.07.026

[11] W. Zhang, Y. H. Hu. Progress in proton-conducting oxides as electrolytes for low-temperature solid oxide fuel cells: from materials to devices. Energy Science & Engineering 9(7) (2021) 984. https://doi.org/10.1002/ese3.886

[12] N. Wang, C. Tang, L. Du, R. Zhu, L. Xing, Z. Song, B. Yuan, L. Zhao, Y. Aoki, S. Ye. Advanced cathode Materials for protonic Ceramic fuel Cells: recent Progress and future Perspectives. Advanced Energy Materials 12(34) (2022) 2201882. https://doi.org/10.1002/aenm.202201882

[13] A. K. Demin, D. I. Bronin. Solid state electrochemical devices for hydrogen energy. Electrochemical Materials and Technologies 2(2) (2023) 20232016. https://doi.org/10.15826/elmattech.2023.2.016
[14] N. A. Danilov, I. A. Starostina, G. N. Starostin, A. V. Kasyanova, D. A. Medvedev, Z. Shao. Fundamental understanding and applications of protonic Y- and Yb-coped Ba(Ce,Zr)O3 Perovskites: State-of-the-art and Perspectives. Advanced Energy Materials 13(47) (2023) 2302175. https://doi.org/10.1002/aenm.202302175
[15] L. A. Dunyushkina, S. A. Belyakov, N. M. Filatov. Proton-conducting alkaline earth hafnates: A review of manufacturing technologies, physicochemical properties and electrochemical performance. Journal of the European Ceramic Society 43(15) (2023) 6681. https://doi.org/10.1016/j.jeurceramsoc.2023.07.011
[16] A. K. Nayak, A. Sasmal. Recent advance on fundamental properties and synthesis of barium zirconate for proton conducting ceramic fuel cell. Journal of Cleaner Production 386 (2023) 135827. https://doi.org/10.1016/j.jclepro.2022.135827
[17] I. A. Zvonareva, D. A. Medvedev. Proton-conducting barium stannate for high-temperature purposes: A brief review. Journal of the European Ceramic Society 43(2) (2023) 198. https://doi.org/10.1016/j.jeurceramsoc.2022.10.049
[18] J. Cao, Y. Ji, Z. Shao. Perovskites for protonic ceramic fuel cells: a review. Energy & Environmental Science 15(6) (2022) 2200. https://doi.org/10.1039/D2EE00132B
[19] M. A. Nur Syafkeena, M. L. Zainor, O. H. Hassan, N. A. Baharuddin, M. H. D. Othman, C. J. Tseng, N. Osman. Review on the preparation of electrolyte thin films based on cerate-zirconate oxides for electrochemical analysis of anode-supported proton ceramic fuel cells. Journal of Alloys and Compounds 918 (2022) 165434. https://doi.org/10.1016/j.jallcom.2022.165434
[20] D. A. Medvedev, J. G. Lyagaeva, E. V. Gorbova, A. K. Demin, P. Tsiakaras. Advanced materials for SOFC application: strategies for the development of highly conductive and stable solid oxide proton electrolytes. Progress in Materials Science 75 (2016) 38. https://doi.org/10.1016/j.pmatsci.2015.08.001
[21] F. J. A. Loureiro, N. Nasani, G. S. Reddy, N. R. Munirathnam, D. P. Fagg. A review on sintering technology of proton conducting BaCeO3-BaZrO3 perovskite oxide materials for protonic Ceramic fuel Cells. Journal of Power Sources 438 (2019) 226991. https://doi.org/10.1016/j.jpowsour.2019.226991
[22] J. Li, C. Wang, X. Wang, L. Bi. Sintering aids for proton-conducting oxides – A double-edged sword? A mini review. Electrochemistry Communications 112 (2020) 106672. https://doi.org/10.1016/j.elecom.2020.106672
[23] J. Tong, D. Clark, L. Bernau, M. Sanders, R. O'Hayre. Solid-state reactive sintering mechanism for large-grained yttrium-doped barium zirconate proton conducting ceramics. Journal of Materials Chemistry 20(30) (2010) 6333. https://doi.org/10.1039/C0JM00381F
[24] D. Han, Y. Otani, Y. Noda, T. Onishi, M. Majima, T. Uda. Strategy to improve phase compatibility between proton conductive BaZr0.8Y0.2O3−δ and nickel oxide. RSC Advances 6(23) (2016) 19288. https://doi.org/10.1039/C5RA26947D
[25] Z. Liu, X. Wang, M. Liu, J. Liu. Enhancing sinterability and electrochemical properties of Ba(Zr0.1Ce0.7Y0.2)O3-δ proton conducting electrolyte for solid oxide fuel cells by addition of NiO. International Journal of Hydrogen Energy 43(29) (2018) 13501. https://doi.org/10.1016/j.ijhydene.2018.05.089
[26] A. M. Dayaghi, J. M. Polfus, R. Strandbakke, A. Pokle, L. Almar, S. Escolástico, E. Vøllestad, J. M. Serra, R. Haugsrud, T. Norby. Effects of sintering additives on defect chemistry and hydration of BaZr0.4Ce0.4(Y,Yb)0.2O3−δ proton conducting electrolytes. Solid State Ionics 401 (2023) 116355. https://doi.org/10.1016/j.ssi.2023.116355
[27] E. Kim, Y. Yamazaki, S. M. Haile, H. I. Yoo. Effect of NiO sintering-aid on hydration kinetics and defect-chemical parameters of BaZr0.8Y0.2O3−Δ. Solid State Ionics 275 (2015) 23. https://doi.org/10.1016/j.ssi.2015.01.001
[28] D. A. Medvedev, A. A. Murashkina, A. K. Demin. Formation of dense electrolytes based on BaCeO3 and BaZrO3 for application in solid oxide fuel cells: the role of solid-state reactive sintering. Review Journal of Chemistry 5(3) (2015) 193. https://doi.org/10.1134/S2079978015030024
[29] S. Yang, Q. Song, L. Chao, D. Li, Y. Wang. Grain characteristics of perovskite Thin films Based on SEM image Segmentation. Advanced Theory and Simulations 7(2) (2024) 2300619. https://doi.org/10.1002/adts.202300619
[30] T. Schober. Water vapor solubility and electrochemical characterization of the high temperature proton conductor BaZr0.9Y0.1O2.95. Solid State Ionics 127(3-4) (2000) 351. https://doi.org/10.1016/S0167-2738(99)00283-0
[31] F. Iguchi, T. Yamada, N. Sata, T. Tsurui, H. Yugami. The influence of grain structures on the electrical conductivity of a BaZr0.95Y0.05O3 proton conductor. Solid State Ionics 177(26-32) (2006) 2381. https://doi.org/10.1016/j.ssi.2006.07.008
[32] S. Duval, P. Holtappels, U. Vogt, E. Pomjakushina, K. Conder, U. Stimming, T. Graule. Electrical conductivity of the proton conductor BaZr0.9Y0.1O3−δ obtained by high temperature annealing. Solid State Ionics 178(25-26) (2007) 1437. https://doi.org/10.1016/j.ssi.2007.08.006

[33] P. Rajasekaran, M. Arivanandhan, Y. Kumaki, R. Jayavel, Y. Hayakawa, M. Shimomura. Facile synthesis of morphology-controlled La:BaSnO3 for the enhancement of thermoelectric power factor. CrystEngComm 22(32) (2020) 5363. https://doi.org/10.1039/D0CE00702A
[34] S. Likhittaphon, T. Pukkrueapun, P. Seeharaj, U. Wetwathana Hartley, N. Laosiripojana, P. Kim-Lohsoontorn. Effect of sintering additives on barium cerate based solid oxide electrolysis cell for syngas production from carbon dioxide and steam. Fuel Processing Technology 173 (2018) 119. https://doi.org/10.1016/j.fuproc.2018.01.019
[35] Z. Leng, Z. Huang, X. Zhou, B. Zhang, H. Bai, J. Zhou, S. Wang. The effect of sintering aids on BaCe0·7Zr0·1Y0.1Yb0.1O3-δ as the electrolyte of proton-conducting solid oxide electrolysis cells. International Journal of Hydrogen Energy 47(79) (2022) 33861. https://doi.org/10.1016/j.ijhydene.2022.07.237
[36] K. Y. Park, Y. Seo, K. B. Kim, S. J. Song, B. Park, J. Y. Park. Enhanced proton conductivity of yttrium-doped barium zirconate with sinterability in protonic ceramic fuel cells. Journal of Alloys and Compounds 639 (2015) 435. https://doi.org/10.1016/j.jallcom.2015.03.168
[37] N. Nasani, Z. Shakel, F. J. A. Loureiro, B. B. Panigrahi, B. B. Kale, D. P. Fagg. Exploring the impact of sintering additives on the densification and conductivity of BaCe0.3Zr0.55Y0.15O3-δ electrolyte for protonic ceramic fuel cells. Journal of Alloys and Compounds 862 (2021) 158640. https://doi.org/10.1016/j.jallcom.2021.158640
[38] M. Amsif, D. Marrero-López, J. C. Ruiz-Morales, S. N. Savvin, P. Núñez. Effect of sintering aids on the conductivity of BaCe0.9Ln0.1O3−δ. Journal of Power Sources 196(22) (2011) 9154. https://doi.org/10.1016/j.jpowsour.2011.06.086
[39] H. I. Ji, B. K. Kim, J. W. Son, K. J. Yoon, J. H. Lee. Influence of sintering activators on electrical property of BaZr0.85Y0.15O3-δ proton-conducting electrolyte. Journal of Power Sources 507 (2021) 230296. https://doi.org/10.1016/j.jpowsour.2021.230296
[40] S. Nikodemski, J. Tong, C. Duan, R. O'Hayre. Ionic transport modification in proton conducting BaCe0.6Zr0.3Y0.1O3−δ with transition metal oxide dopants. Solid State Ionics 294 (2016) 37. https://doi.org/10.1016/j.ssi.2016.06.020
[41] G. Vdovin, A. Rudenko, B. Antonov, V. Malkov, A. Demin, D. Medvedev. Manipulating the grain boundary properties of BaCeO3-based ceramic materials through sintering additives introduction. Chimica Techno Acta 6(2) (2019) 38. https://doi.org/10.15826/chimtech.2019.6.2.01
[42] M. A. Azimova, S. McIntosh. Transport properties and stability of cobalt doped proton conducting oxides. Solid State Ionics 180(2-3) (2009) 160. https://doi.org/10.1016/j.ssi.2008.12.013
[43] S. Ricote, N. Bonanos. Enhanced sintering and conductivity study of cobalt or nickel doped solid solution of barium cerate and zirconate. Solid State Ionics 181(15-16) (2010) 694. https://doi.org/10.1016/j.ssi.2010.04.007
[44] D. Medvedev, V. Maragou, T. Zhuravleva, A. Demin, E. Gorbova, P. Tsiakaras. Investigation of the structural and electrical properties of Co-doped BaCe0.9Gd0.1O3−δ. Solid State Ionics 182(1) (2011) 41. https://doi.org/10.1016/j.ssi.2010.11.008
[45] R. M. German, P. Suri, S. J. Park. Review: liquid phase sintering. Journal of Materials Science 44(1) (2009) 1. https://doi.org/10.1007/s10853-008-3008-0
[46] R. B. Heady, J. W. Cahn. An analysis of the capillary forces in liquid-phase sintering of spherical particles. Metallurgical Transactions 1(1) (1970) 185. https://doi.org/10.1007/BF02819260
[47] J. J. Lander. The phase System BaO-NiO. Journal of the American Chemical Society 73(6) (1951) 2450. https://doi.org/10.1021/ja01150a012
[48] G. N. Starostin, M. T. Akopian, G. K. Vdovin, I. A. Starostina, G. Yang, D. A. Medvedev. Transport properties of highly dense proton-conducting BaSn1−xInxO3−δ ceramics. International Journal of Hydrogen Energy 69 (2024) 306. https://doi.org/10.1016/j.ijhydene.2024.05.012
[49] G. N. Starostin, M. T. Akopian, I. A. Starostina, D. A. Medvedev. Co-doping effect on the microstructural and electrical properties of barium stannate materials. Electrochemical Materials and Technologies 3(3) (2024) 20243037. https://doi.org/10.15826/elmattech.2024.3.037
[50] J. Tong, D. Clark, L. Bernau, A. Subramaniyan, R. O'Hayre. Proton-conducting yttrium-doped barium cerate ceramics synthesized by a cost-effective solid-state reactive sintering method. Solid State Ionics 181(33-34) (2010) 1486. https://doi.org/10.1016/j.ssi.2010.08.022
[51] N. Nasani, D. Pukazhselvan, A. V. Kovalevsky, A. L. Shaula, D. P. Fagg. Conductivity recovery by redox cycling of yttrium doped barium zirconate proton conductors and exsolution of Ni-based sintering additives. Journal of Power Sources 339 (2017) 93. https://doi.org/10.1016/j.jpowsour.2016.11.036
[52] M. Knight, D. Jennings, S. Ricote, I. Reimanis. Estimating ni valence with magnetometry in solid-state reactive sintered yttrium-doped barium zirconate. Journal of the American Ceramic Society 105(1) (2022) 159. https://doi.org/10.1111/jace.18084

[53] M. Wang, E. I. Papaioannou, I. S. Metcalfe, A. Naden, C. D. Savaniu, J. T. S. Irvine. The exsolution of cu Particles from doped Barium cerate Zirconate via barium Cuprate intermediate Phases. Advanced Functional Materials 33(27) (2023) 2302102. https://doi.org/10.1002/adfm.202302102
[54] J. J. Lander. The phase System BaO-NiO. Journal of the American Chemical Society 73(6) (1951) 2450. https://doi.org/10.1021/ja01150a012
[55] A. S. Urusova, V. A. Cherepanov, T. V. Aksenova, L. Y. Gavrilova, E. A. Kiselev. Phase equilibria, crystal structure and oxygen content of intermediate phases in the Y–Ba–Co–O system. Journal of Solid State Chemistry 202 (2013) 207. https://doi.org/10.1016/j.jssc.2013.03.037
[56] T. Shimura, H. Tanaka, H. Matsumoto, T. Yogo. Influence of the transition-metal doping on conductivity of a BaCeO3-based protonic conductor. Solid State Ionics 176(39-40) (2005) 2945. https://doi.org/10.1016/j.ssi.2005.09.027
[57] J. Basu, A. Suresh, B. A. Wilhite, C. B. Carter. Microstructural evolution of cobalt-doped barium cerate–zirconate at elevated temperatures under moist reducing conditions. Journal of the European Ceramic Society 31(8) (2011) 1421. https://doi.org/10.1016/j.jeurceramsoc.2011.02.029
[58] L. Yang, S. Wang, X. Lou, M. Liu. Electrical conductivity and electrochemical performance of cobalt-doped BaZr0.1Ce0.7Y0.2O3−δ cathode. International Journal of Hydrogen Energy 36(3) (2011) 2266. https://doi.org/10.1016/j.ijhydene.2010.11.053
[59] G. Accardo, D. Frattini, S. P. Yoon. Enhanced proton conductivity of Gd–co bi-doped barium cerate perovskites based on structural and microstructural investigations. Journal of Alloys and Compounds 834 (2020) 155114. https://doi.org/10.1016/j.jallcom.2020.155114
[60] C. Schmetterer, H. Flandorfer, K. W. Richter, H. Ipser. Phase equilibria in the Ag-Ni-sn System: isothermal Sections. Journal of Electronic Materials 36(11) (2007) 1415. https://doi.org/10.1007/s11664-007-0205-6
[61] P. Nash, H. Choo, R. B. Schwarz. Thermodynamic Calculation of Phase Equilibria in the Ti–Co and Ni–Sn Systems. Journal of Materials Science 33(20) (1998) 4929. https://doi.org/10.1023/A:1004478101233
[62] C. Jin, Z. Huizhu, D. Lei, L. Yuehua, L. Wang. Effect of ba nonstoichiometry on the phase composition, microstructure, chemical stability and electrical conductivity of BaxCe0.7Zr0.1Y0.1Yb0.1O3−δ (0.9≤x≤1.1) proton conductors. Ceramics International 41(6) (2015) 7796. https://doi.org/10.1016/j.ceramint.2015.02.113
[63] W. Yang, H. Zhou, L. Wang, Y. Li, Z. He, C. Han, L. Dai. The influence of Ba-site non-stoichiometry on the phase composition, sinterability, conductivity and chemical stability of BaxZr0.6Hf0.2Y0.2O3-δ (0.9≤x≤1.03) proton conductors. International Journal of Hydrogen Energy 46(18) (2021) 10838. https://doi.org/10.1016/j.ijhydene.2020.12.167
[64] Y. Guo, R. Ran, Z. Shao, S. Liu. Effect of ba nonstoichiometry on the phase structure, sintering, electrical conductivity and phase stability of Ba1±xCe0.4Zr0.4Y0.2O3−δ (0≤x≤0.20) proton conductors. International Journal of Hydrogen Energy 36(14) (2011) 8450. https://doi.org/10.1016/j.ijhydene.2011.04.037
[65] A. M. Mineev, I. A. Zvonareva, D. A. Medvedev, Z. Shao. Maintaining pronounced proton transportation of solid oxides prepared with a sintering additive. Journal of Materials Chemistry A 9(25) (2021) 14553. https://doi.org/10.1039/D1TA03399A
[66] I. A. Starostina, G. N. Starostin, M. T. Akopian, G. K. Vdovin, D. A. Osinkin, B. Py, A. Maradesa, F. Ciucci, D. A. Medvedev. Insight into grain and Grain-boundary Transport of Proton-conducting Ceramics: A case Report of BaSn0.8Y0.2O3−δ. Advanced Functional Materials 34(6) (2024) 2307316. https://doi.org/10.1002/adfm.202307316
[67] G. Gregori, R. Merkle, J. Maier. Ion conduction and redistribution at grain boundaries in oxide systems. Progress in Materials Science 89 (2017) 252. https://doi.org/10.1016/j.pmatsci.2017.04.009
[68] Y. Y. Sun, Q. Zhang, L. Yan, T. B. Wang, P. Y. Hou. A review of interfaces within solid-state electrolytes: fundamentals, issues and advancements. Chemical Engineering Journal 437 (2022) 135179. https://doi.org/10.1016/j.cej.2022.135179
[69] L. Zhang, Y. Pu, M. Chen. Complex impedance spectroscopy for capacitive energy-storage ceramics: a review and prospects. Materials Today Chemistry 28 (2023) 101353. https://doi.org/10.1016/j.mtchem.2022.101353
[70] N. Kochetova, I. Animitsa, D. Medvedev, A. Demin, P. Tsiakaras. Recent activity in the development of proton-conducting oxides for high-temperature applications. RSC Advances 6(77) (2016) 73222. https://doi.org/10.1039/c6ra13347a
[71] Y. Wan, B. He, R. Wang, Y. Ling, L. Zhao. Effect of co doping on sinterability and protonic conductivity of BaZr0.1Ce0.7Y0.1Yb0.1O3−δ for protonic ceramic fuel cells. Journal of Power Sources 347 (2017) 14. https://doi.org/10.1016/j.jpowsour.2017.02.049